Research Article

Orhan Kaya*, Alparslan Oztekin, Edmund B. Webb III

Development of AMBER-compliant transferable force field parameters for polytetrafluoroethylene

https://doi.org/10.1515/chem-2024-0072
received May 14, 2024; accepted July 23, 2024

Abstract: New transferable parameters for polytetrafluoroethylene (PTFE) compatible with the Assisted Model Building with Energy Refinement (AMBER) force field were developed by including many conformational states to improve accuracy. The Austin–Frisch–Petersson functional with dispersion hybrid density functional theory, advantageous for treating dispersion, was used to obtain quantum mechanical reference data. The restrained electrostatic potential method was used to compute the partial charges. The bonds, angles, and dihedral parameters were obtained via Paramfit software fitted to quantum mechanical data. The optimization of van der Waals parameters was obtained in the condensed phase through molecular dynamics simulations and the simplex method. These parameters were transferred to various molecular weights of PTFE assembly systems to calculate the density, radial distribution functions, power spectrum, and specific heat capacity. The highest percent error in density was 1.4% for the modeled PTFE ensembles. The calculated vibrational spectrum peaks closely matched experimental peaks with a maximum wavenumber deviation of 19 cm^{-1}. The highest percent error to specific heat capacity was 5%. These results represent a significant improvement over pre-existing potentials in the literature and provide parameters that can be used to model PTFE in many existing simulation codes.

Keywords: polytetrafluoroethylene, AMBER force field, parameter optimization, molecular dynamics simulation, density functional theory

*** Corresponding author: Orhan Kaya**, Department of Mechanical Engineering and Mechanics, Lehigh University, Bethlehem, Pennsylvania 18015, United States of America, e-mail: ork216@lehigh.edu
Alparslan Oztekin, **Edmund B. Webb III:** Department of Mechanical Engineering and Mechanics, Lehigh University, Bethlehem, Pennsylvania 18015, United States of America

1 Introduction

Polytetrafluoroethylene (PTFE) has a variety of commercial uses, particularly in engineering and medicine. Engineering research and applications involving PTFE cover a wide range of fields, such as membrane distillation application [1], semiconductor industry [2], and enhanced coating [3]. PTFE also finds extensive applications in various medical fields, such as dental prostheses and devices [4], hydrophobic acrylic equiconvex intraocular lenses [5], drug delivery [6], and blood substitutes [7], among others. PTFE is preferred in many other nano research fields because it is hydrophobic, thermally stable, inert, and non-toxic; it has a low friction coefficient, dielectric coefficient, and high surface resistance [8]. In PTFE applications, we may encounter poorly understood molecular behavior, such as short-lived interaction and unstable intermediates, as well as transition states that are impossible to observe experimentally [8,9]. The molecular design of PTFE materials is essential to improve PTFE applications and understand behavior at the nano-scale.

The need for an accurate PTFE force field has prompted prior work by some research groups. PTFE force field parameters available in the literature are dedicated to solving challenging problems related to experiments and reproducing experimental and theoretical data with the highest degree of accuracy. However, they usually produce some shortcomings. Okada et al. [10] developed an all-atom PTFE model using a molecular dynamics (MD) calculation package GEMS/MD for the reference molecules of perfluoroalkanes, including *n*-C_3F_8, *n*-C_4F_{10}, and *n*-C_6F_{14}; they utilized the HF/6-31G *ab initio* method, omitting the electron correlation effect [11,12]. The charges were derived using experimental dipole moment data. The bond, angle, and dihedral parameters were derived using the first principles method. They optimized the van der Waals (vdW) parameters by adding artificial nonbonding potentials between atoms separated by four bonds at positions 1–5 (vdW_{1-5}). They claimed that the "1–5" interactions involving long PTFE chains are significant because the attractive interactions between

fluorine atoms at these positions can affect the molecule's conformation and properties. However, articles published later showed that the PTFE chain helix, affected by the artificial vdW_{1-5} potential functions between an atom and its fourth bond partner, did not adequately describe the energy landscape. While the *trans* conformations (t^+, t^-) closely matched the theoretical calculation results, the energy plot generated using the force field parameters failed to reproduce gauche conformations (g^+, g^-).

Jang et al. [13] developed a new Dreiding-type valence potential set for analyzing vdW_{1-5} non-bond interactions and predicted helical conformations. They conducted B3LYP\6-31G* [14,15] model chemistry employing the Hessian-biased singular-value decomposition technique [16] to derive bonds, angles, torsional, and molecular vibrational frequency parameters with Dreiding functional form by including many effects of electron correlation except treatment of dispersion. The charges were derived with Mulliken population atomic point charges [17]. They compared energy-minimized conformations between reference data and the force field of longer per-fluorinated alkanes. The authors concluded that Coulomb repulsion is the dominant helicity source for the all-*trans* conformations. They predicted the correct helical minima with t^+, t^-, and helical (h^+, h^-) conformations. However, at the onset of bending torsional angle values, the g^+ and g^- conformational sets proved unstable.

Watkins and Jorgensen [18] proposed another all-atom parameter set for PTFE molecules. They derived the force field for PTFE using OPLS functional form; their quantum mechanical data were generated using the LMP2/cc-pVTZ ($^{-f}$) [12,19] and HF/6-31G* [11,12] theoretical method that adds corrections to achieve superior accuracy for electron correlation without treatment of dispersion. Despite good predictions of densities and heat of vaporization, Borodin et al. [20] showed that the transferability of the *n*-C_4F_{10} and *n*-C_5F_{12} could not adequately define conformational energetics by using the same torsional parameters. Thus, Borodin et al. derived bonds, angles, and nonbonded parameters using MP2/aug-cc-pvDz [12,21] and B3LYP/D95+* [12,14] model chemistry. They provided a satisfactory description of the transferability for *n*-C_4F_{10} and *n*-C_5F_{12} but exhibited notably less precise thermodynamic data, encompassing density and heat of vaporization.

The general AMBER force field (GAFF) [22] database contains parameters for numerous polymers, including PTFE. Bhowmik et al. [23] concluded that the standard GAFF necessitates parameter tuning to precisely predict specific heat across various polymers, PTFE included.

Consequently, providing a comprehensive description of PTFE solely based on force field parameters proves challenging. As indicated above, various studies have created new force field parameters. Still, they faced difficulties representing all conformational states, achieving transferability accuracy, obtaining precise thermodynamics (density, heat of vaporization), and generating more reliable charge parameters. To overcome inconsistencies in PTFE parameterizations in the literature, we developed Assisted Model Building with Energy Refinement (AMBER)-compliant transferable force field parameters for PTFE by carrying out the advanced APFD\6-31G* [12,24] model chemistry to characterize a large set of conformational states. The Austin–Frisch–Petersson functional with dispersion (APFD) hybrid density functional theory method involving the dispersion process is susceptible to the integration grid and generally requires finer grids than other functionals to achieve reasonable numerical stability [9]. Including electron correlation effects and considering both core and valence electrons contribute to more reliable and superior performance for a range of compounds than B3LYP [25,26]. The atomic partial charges were obtained through the restrained electrostatic potential (RESP) method [27] using Gaussian 16 version [28] and Antechamber software [29] packages. The paramfit program [30] was utilized for deriving bond, angle, and dihedral parameters to fit quantum mechanical reference data of 29 conformational sets of *n*-C_4F_{10} reference molecules. The vdW interactions were optimized based on condensed phase heat of vaporization and density values. Using the force field parameters, MD simulations were conducted using a system of 50 reference molecules of *n*-C_4F_{10}. The findings demonstrated that the experimental values of density and heat of vaporization were accurately reproduced. Then, the force field parameters were transferred to simulate different molecular weights of PTFE to calculate density, power spectrum, and specific heat capacity. The potential advanced here demonstrates very good agreement with experimental measurements [31–34], and it shows notable improvement in the accuracy of its predictions compared to pre-existing interatomic potentials for PTFE reported in the literature [10,13,18,20,22].

2 Parameterization methods

2.1 AMBER interaction model

The AMBER interaction model, presented below, describes the potential energy of a molecular system [22].

$$E = \sum_{\text{bond}} K_r(r - r_{\text{eq}})^2 + \sum_{\text{angle}} K_\theta(\theta - \theta_{\text{eq}})^2 + \sum_{\text{torsion}} \frac{v_n}{2}[1 + \cos(n\varphi - \gamma)] + \sum_{\text{nonbond}}^{i<j} \varepsilon_{ij}\left[\left(\frac{\sigma_{ij}}{r_{ij}}\right)^{12} - 2\left(\frac{\sigma_{ij}}{r_{ij}}\right)^{6}\right] + \sum_{\text{nonbond}}^{i<j} \frac{q_i q_j}{r_{ij}}. \quad (1)$$

K_r, K_θ, and v_n represent the force constants for the bonded terms. r_{eq} is the equilibrium bond length; θ_{eq} is the equilibrium bond angle. n is the multiplicity of the associated torsion angle, γ is the phase angle, and φ is the equilibrium torsion angle. ε_{ij} is the energy well depth of the vdW interaction, r_{ij} is the distance between nonbonded atoms i and j, and σ_{ij} is the distance parameter of the Lennard–Jones (LJ) 12-6 function. In the final nonbonding term, q_i and q_j represent atomic charges.

In brief, the parameterization was performed using the following procedure: preliminarily, the atom types and the n-C_4F_{10} reference molecule were modeled in .pdb format files using the Avogadro Molecular Editor [35]. Then, the parameter file for the force field was prepared, including all parameters to be fitted. The conformational sets were generated using Gaussian 16 [28] by specifying which dihedral angle to scan while relaxing other coordinates from an optimized n-C_4F_{10} reference molecule; it was ensured that conformations spanned a considerable range in energy, including a few at high energy (Figure 3a). The paramfit tool was employed to fit all of the parameters in the conformational sets of bonded terms. Then, the LJ potentials were optimized using experimental data of the n-C_4F_{10} reference molecule. Details about each of these steps are provided in the following sections. The quality of the parameter set was thoroughly examined and evaluated to ensure reasonable accuracy was obtained for all generated structures across the sampled conformational space.

2.2 Charge optimization

The atomic partial charges were obtained from QM wave functions and fitted to electron density and potential. Gaussian 16 was utilized to generate the electron density and electrostatic potential (ESP) at various points around the structure of isolated n-C_4F_{10} molecules at the APFD\6-31G* level model chemistry and the corresponding optimized structure was directed to Antechamber to produce charges. The APFD\6-31G* method was chosen because it provides more reliable and superior performance for a range of compounds than B3LYP [25,26].

2.3 Bond, angle, and dihedral optimization

The Paramfit program [36] was utilized to derive force field parameters for bonded interaction terms by employing the least-squares method to minimize discrepancies between the molecular mechanics (MM) calculation using the present force field and QM energies [37]. The sets of conformations formed by the n-C_4F_{10} structure in Figure 1 have 13 bonds: 3 C–C bonds, 10 C–F bonds, and 3 atom types assigned. The C–C bonds exhibit symmetry, while C–F bonds fall into two different groups, one corresponding to two fluorines bonded to the central carbon (CF_2) and the other corresponding to three fluorines bonded to the triple carbons (CF_3) [38].

The 32 sets of *trans* and *gauche* conformations of the n-C_4F_{10} structure were generated by sampling dihedral angles at 15° intervals. We performed relaxed sampling at each specified dihedral angle to obtain more precise potential energy profiles, permitting all other internal coordinates to relax. These angles, defined for the carbon atoms in the reference molecule, ranged from 0° to 180°. Next, calculations for single-point energy and energy gradients were conducted for these conformations using APFD\6-31G* level theory. The conformations that result in duplicate QM energies were identified. Only one representative conformation was retained for further analysis; the others were excluded. This reduced the set of 32 to 29 *trans* and *gauche* conformations. Twenty-nine conformations combined 377 data points for bonds, 696 for angles, and 783 for dihedrals. The data points were employed to fit the AMBER energies to the quantum energies. The following minimization equation was used:

$$\sum_{i=1}^{N} w_i[(E_{\text{MM}}(i) - E_{\text{QM}}(i))^2 + K] = 0, \quad (2)$$

where K represents the internal inconsistency between quantum and AMBER energies for the system, and N stands for the number of data points corresponding to bonds, angles, and dihedrals, respectively. w_i is a weight

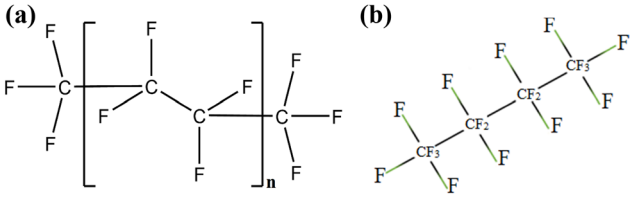

Figure 1: (a) The molecular structure of PTFE consists of long chains with repeating units of tetrafluoroethylene (*n* units), as indicated in parentheses. (b) A bond schematic of the reference molecule is to be parameterized.

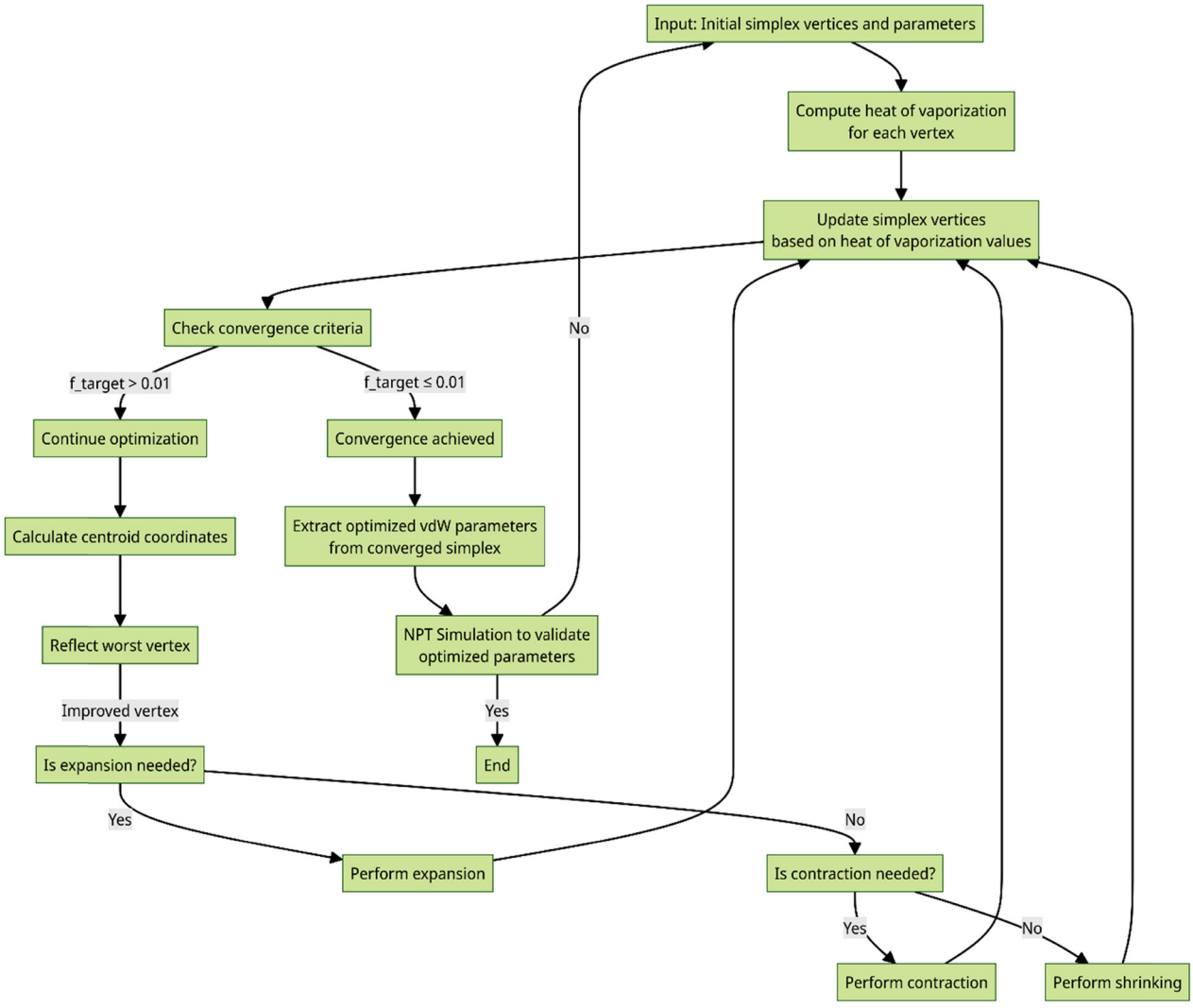

Figure 2: A schematic representation of the update mechanisms within the simplex optimization algorithm.

set to 1 by default. The goal is to iteratively solve equation (2) while minimizing each value of K (i.e., K_{bonds}, K_{angles}, and $K_{\text{dihedrals}}$). During each iteration of the minimization process, Paramfit optimized the objective functions with the combination of K_{bonds}, K_{angles}, and $K_{\text{dihedrals}}$ to determine K values for bonds, angles, and dihedrals, respectively, aiming to minimize potential energy errors across conformational sets compared to quantum reference data. Then, the determined K_{bonds}, K_{angles}, and $K_{\text{dihedrals}}$ values were used for the entire data sets for bonds, angles, and dihedrals to fit the force field parameters. These minimization steps quantified the fit quality of MM equilibrium bonds, angles, and dihedral values, enabling the force field to provide reliable predictions for all 29 conformational sets. The conformational energies computed from the MM force field were compared to QM reference values to measure the accuracy of the final bonded interaction parameter values. Additionally, all bond lengths, angles, and dihedral angles obtained from the MM force field were compared to their QM counterpart values. The average absolute deviation (AAD) was computed for all quantities or traits and compared:

$$\text{AAD} = \frac{\sum_{t=1}^{N} |\text{QM}_t - \bar{\text{MM}}_t|}{N}. \tag{3}$$

The root-mean-square deviation (RMSD) was also calculated.

$$\text{RMSD} = \sqrt{\frac{\sum_{t=1}^{N} (\text{QM}_t - \text{MM}_t)^2}{N}}. \tag{4}$$

Four pairs of AAD and RMSD values were computed, one pair each from the conformational energies, bond lengths, bond angles, and dihedral angles. In the two preceding equations, QM_t is a quantum mechanics reference

value for the given trait t, MM_t is the corresponding molecular mechanics calculated value, and N denotes the total number of data points for each trait (N = 29 for conformation energies, 377 for bond lengths, 696 for bond angles, and 783 for dihedral angles).

2.4 vdW optimization

We employed a combination of MD simulations using the GROMACS simulation package [39] and a simplex fitting procedure to optimize the vdW parameters for the PTFE reference molecule in condensed phases. The optimization process utilized experimental data of liquid density as 1.6 g/cm^3 [18,31], and heat of vaporization as 5.46 kcal/mol [18,31]; the former property is susceptible to vdW length parameters and the latter to the energy parameters. In all fluid simulations, cubic boxes with periodic boundary conditions were used, and each cell contained 50 reference molecules of n-C_4F_{10}. The dimensions of the cubic box were set to have cell sides measuring 25 Å, and then the cell and coordinates were compressed to give experimental density. Once the initial configurations of the 50 reference molecules of n-C_4F_{10} to be simulated were established, the optimization of the vdW was performed using the following procedure.

The fitting process involves creating a simplex with N vertices in an n-dimensional parameter space. Each vertex is represented by a vector $x_i = (x_{i1}, x_{i2},..., x_{in})$, where i ranges from 1 to N. The six LJ force field parameters (ε_F, σ_F, ε_{CF2}, σ_{CF2}, ε_{CF3}, σ_{CF3}) for three atom types (F, CF_2, and CF_3) indicate, here, n = 6. In the six-dimensional parameter space, an initial simplex with seven vertices (Table 1) was formed using the Nelder–Mead algorithm [40]. Each parameter was bounded as (0, 5) for all vertices defined. These bounds also define the range within which the parameters can be adjusted during optimization.

In Table 1, δ is a small perturbation from the initial values and is set to 0.1 in this study. The optimization process has the following steps: 1: The system energy was minimized employing the vertex 1 parameter set for 10,000 steps using the steepest descent algorithm, followed by 1 ns NVT (constant number of particles N, volume V, and temperature T = 273 K) simulation to equilibrate the system further. 2: The equilibrated system was subsequently run in a sequence of short (20 ps) NVT simulations to test whether thermodynamic properties converged. 3: This was followed by a final data production NVT simulation for 100 ps, during which heat of vaporization was computed every 20 ps to allow for time averaging. These three steps were performed for each vertex. 4: The objective function, shown in equation (5) from the study of Faller et al. [41], was used to quantify the discrepancy between computed and target values of the heat of vaporization for each vertex.

Table 1: Initial simplex has seven vertices in the parameter space

Vertex 1:	(ε_F, σ_F, ε_{CF2}, σ_{CF2}, ε_{CF3}, σ_{CF3})
Vertex 2:	($\varepsilon_F + \delta$, σ_F, ε_{CF2}, σ_{CF2}, ε_{CF3}, σ_{CF3})
Vertex 3:	(ε_F, $\sigma_F + \delta$, ε_{CF2}, σ_{CF2}, ε_{CF3}, σ_{CF3})
Vertex 4:	(ε_F, σ_F, $\varepsilon_{CF2} + \delta$, σ_{CF2}, ε_{CF3}, σ_{CF3})
Vertex 5:	(ε_F, σ_F, ε_{CF2}, $\sigma_{CF2} + \delta$, ε_{CF3}, σ_{CF3})
Vertex 6:	(ε_F, σ_F, ε_{CF2}, σ_{CF2}, $\varepsilon_{CF3} + \delta$, σ_{CF3})
Vertex 7:	(ε_F, σ_F, ε_{CF2}, σ_{CF2}, ε_{CF3}, $\sigma_{CF3} + \delta$)

$$f_{\text{target}}(\{\text{Vertex}_n\}) = \left\{ w \left[1 - \frac{\Delta H_{\text{vap}}(\{\text{Vertex}_n\})}{\Delta H_{\text{vap,target}}} \right] \right\}^{2}^{1/2}, \quad (5)$$

where w is the weight factor (set equal to 1 throughout this process), $\Delta H_{\text{vap,target}}$ is the experimental value of heat of vaporization, and $\Delta H_{\text{vap}}(\{\text{Vertex}_n\})$ is the heat of vaporization value obtained from the parameters at Vertex_n.

The heat of vaporization was calculated from

$$\Delta H_v = E_i + RT, \quad (6)$$

where E_i represents the total internal energy of the system for the ith vertex, R is the gas constant, and T is the temperature. The process of simplex optimization is depicted schematically in Figure 2. The vertices except the vertex with the highest objective function value (the worst vertex) were modified based on their objective function values and using the reflection, expansion, contraction, and shrinking operations [40–42] described below; all six parameters in the vertices were adjusted simultaneously. The next step is a production stage to define new parameters for the vertices. These update operations continue the movement of the vertices in the parameter space until the convergence criterion ($f_{\text{target}}(\{\text{Vertex}_n\}) \le 0.01$) is achieved. The simplex update procedures carried out in these operations are shown in Table 2. It is important to note that the system box, previously equilibrated with the old parameters at each production stage, is no longer equilibrated with the new parameters. Thus, the system box must be re-equilibrated using the newly obtained vertex parameter sets to achieve a stable configuration.

The simplex update procedure is iterative; j in Table 2 refers to the iteration number. First, the centroid coordinates are calculated by averaging the coordinates of all vertices, except the worst vertex coordinates denoted as $x_w = (x_{w1}, x_{w2}, ..., x_{w6})$. Here, we consider a simplex with

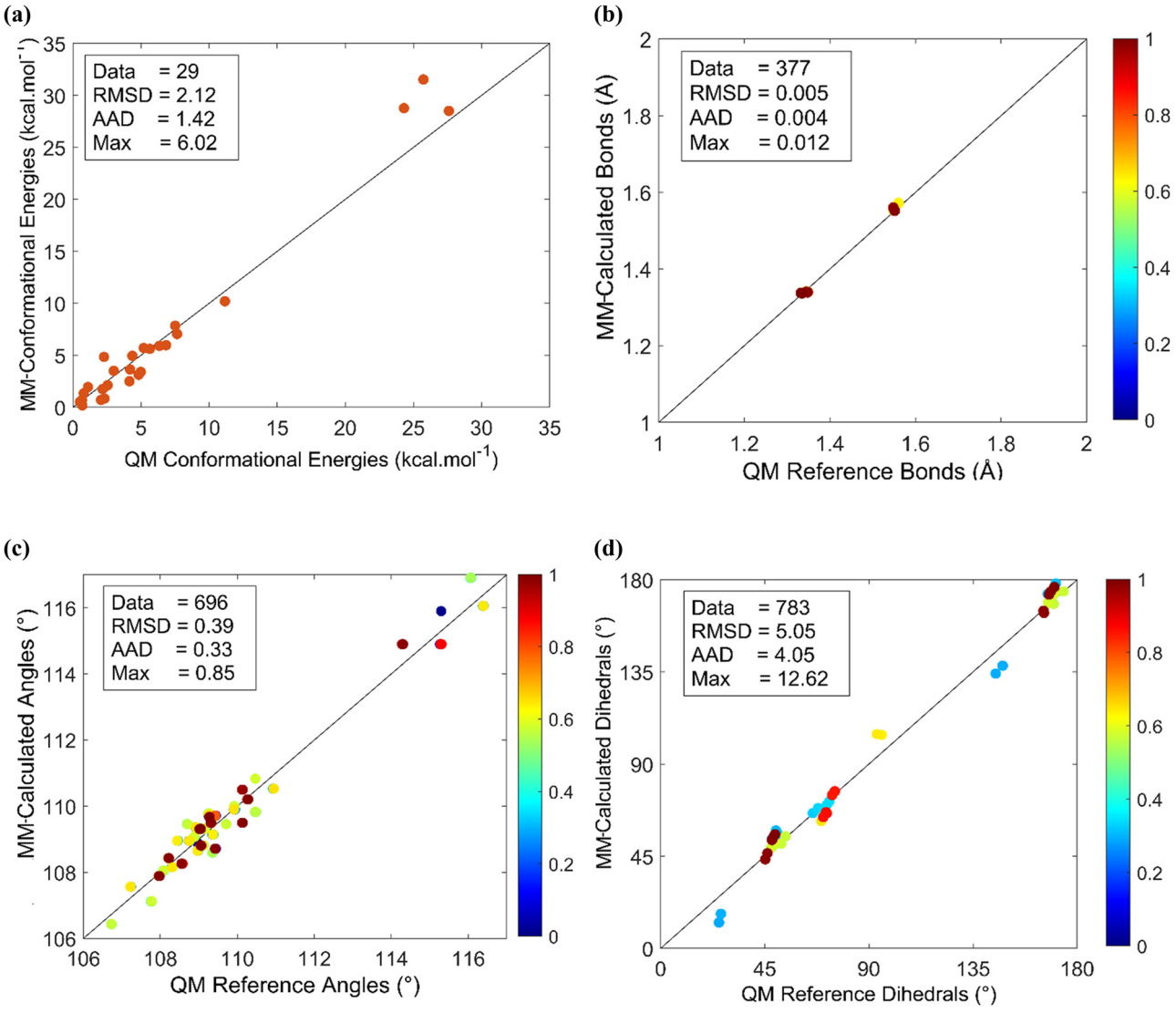

Figure 3: (a) Comparison between MM-calculated results and QM conformational energies across 29 conformational sets is presented. The comparison of bond lengths (b), bond angles (c), and dihedral angles (d) between MM-calculated results and QM reference values is shown, along with the total number of data points (Data), RMSD, AAD, and maximum value differences (Max). The color bar to the right of the plots shows the relative density of the data points (%).

N vertices in a six-dimensional parameter space; each vertex is represented by a vector $x_i = (x_{i1}, x_{i2}, ..., x_{i6})$, where i ranges from 1 up to N, where N denotes the total number of vertices in the simplex. In the centroid coordinate equation illustrated in Table 2, the sum of the coordinate values for all vertices except the worst vertex (the highest objective function value) is divided by (N–1). Applying the equation to each coordinate j, we can compute the centroid coordinates as (c = (c_1, c_2..., c_n)) for the simplex. Then, each operation continues with the reflection of the vertex with the highest objective value. For each coordinate j, the reflected coordinate r_j can be computed using the equation in Table 2. Applying the equation to each coordinate j, we can compute the reflected point coordinates r = (r_1, r_2,..., rn) for the worst vertex. An expansion operation is

Table 2: Simplex update operations and their equations in the parameter space

Operations:	Equations
Centroid (c_j):	$c_j = (x_{1j} + x_{2j} + ... + x_{\{N-1\}j})/(N-1)$
Reflection (r_j):	$r_j = c_j + (c_j - x_{wj})$
Expansion (e_j):	$e_j = \gamma \times r_j + (1-\gamma) \times c_j$
Contraction (co_j):	$co_j = \beta \times x_{wj} + (1-\beta) \times c_j$
Shrinking (s_{ij}):	$s_{ij} = \delta \times x_{bj} + (1-\delta) \times x_{ij}$

performed if the reflected vertex has a lower objective function value (i.e., better). For each coordinate j, the expanded coordinate e_j can be computed using the equation in Table 2. In this equation, γ represents the expansion coefficient, dictating the magnitude of the expansion. Typically, γ is chosen to be greater than 1 (the value is set to $\gamma = 2$ in this research) to move the expanded point further away from the centroid. Applying this equation to each coordinate j, we can compute the expanded point coordinates $e = (e_1, e_2,..., e_n)$ based on the reflected point and centroid. If the expanded point (or vertex) does not improve significantly or has a higher objective function value than the second-worst vertex, the contraction operation was performed according to the equation in Table 2. In this equation, β is the contraction coefficient, which determines the extent of the contraction. Typically, β is chosen to be less than 1 ($\beta = (\pm)0.5$ in this research) to move the contracted point closer to the centroid. Applying this equation to each coordinate j, we can compute the contracted point coordinates $c_o = (c_{o1}, c_{o2},..., c_{on})$ based on the worst vertex and centroid. The shrinking operation is performed if none of the above operations result in a better vertex. To do this, we shrink all vertices of the simplex toward the best vertex (the vertex with the lowest objective function value). We consider the best vertex coordinates as $x_b = (x_{b1}, x_{b2},..., x_{b6})$ and the coordinates of each vertex in the simplex as $x_i = (x_{i1}, x_{i2},..., x_{i6})$. For each vertex i and coordinate j, the shrunk coordinate s_{ij} can be computed using the equation in Table 2. In this equation, δ is the shrinking coefficient, which determines the extent of the shrinking; note that δ used in shrinking is distinct from δ in Table 1. Typically, δ is chosen to be less than 1 (we set it to $\delta = 0.015$) to move the vertices closer to the best vertex. Applying this equation to every vertex i and coordinate j, we can determine the shrunk coordinates s_{ij} for all the simplex vertices.

This optimization process involves iteratively updating the vertices of the simplex based on the objective function evaluations until the convergence criterion ($f_{\text{target}}(\{\text{Vertex}_n\}) \leq 0.01$) was achieved. Then, the final simplex vertex is determined by the coordinates of each parameter (ε and σ) for each atom type (F, CF_2, CF_3). The optimized force field parameters were extracted from the converged simplex. These parameters represent optimal values aimed at minimizing the discrepancy between the calculated and reference values of the heat of vaporization. Following the acquisition of vdW parameters, an NPT simulation lasting 200 ps reached equilibrium after 50 ps at a temperature of 273 K and a pressure of 1 bar. This simulation aimed to assess the density and heat of vaporization to validate the optimized parameters.

3 Parameterization outcomes

3.1 Charge parameters

We successfully determined the RESP charge parameters for the n-C_4F_{10} reference molecule for the F, CF_3, and CF_2 atom types. The RESP charge fitting process involved two main steps: QM calculations and charge optimization. We used APFD\6-31G* QM calculations to generate the ESP. Then, we used the Antechamber program to reproduce the same potential at the MM level by fitting the MM ESP to the QM ESP to minimize the deviation between the computed and target ESP values. Antechamber subsequently generated a file containing the RESP charges for each atom in the n-C_4F_{10} reference molecule, as shown in Table 3. The RESP charge parameters indicate that F in the n-C4F10 molecule is negatively charged with $q = -0.11018$. This result is consistent with the electronegativity of F [43]. On the other hand, C in CF_3 groups are positively charged with $q = 0.33040$, while C in CF_2 groups are also positively charged with $q = 0.22050$.

3.2 Bonds, angles, and dihedral parameters

Paramfit software minimizes the objective function, deriving MM bonds, angles, and dihedral parameters relative to QM reference data. The optimization iterations were performed until the best combination of K_{bonds}, K_{angles}, and $K_{\text{dihedrals}}$ were obtained (i.e., when the objective function provided the lowest potential energy error across all data compared to the previous one). The convergence criterion proposed in Paramfit was used to validate the quality of the entire data parameter set at the final target K values. Figure 3(a) compares the MM energies of the 29 conformational sets obtained with the QM energies. A good agreement exists between MM and QM results; a more significant discrepancy exists for a few conformations, but the overall matching was considered satisfactory. All the MM-calculated results of bond lengths, bond angles, and dihedral angles were generated using the final force field parameter set after minimizing the objective function for all sets of geometries. These results were then

Table 3: Optimized charge parameters for PTFE

Charge	Atom types	q(e)
F	F	−0.11018
C	CF_3	0.33040
C	CF_2	0.22050

compared to their QM-derived counterpart values. The MM bond length values exhibited excellent agreement with the QM values, with all cases not exceeding 0.1 Å difference (Figure 3(b)). Similarly, for the bond angles in Figure 3(c), discrepancies between MM and QM results did not exceed $\pi/20$ radians. Furthermore, the MM dihedrals data sets in Figure 3(d) showed agreement within $\pi/10$ radians across all data and conformational sets compared to the quantum reference data.

Given the overall satisfactory agreement between MM and QM calculations across such a wide range of conformations, the final equilibrium bond length r_{eq} and bond force constant K_r, equilibrium angle θ_{eq} and angle force constant K_θ, dihedral barrier height v_n, dihedral phase γ and periodicity n shown in Tables 4–6 were then calculated.

The relative conformational energies of n-C_4F_{10}, ranging from 0° to 180° as shown in Figure 4, were compared using advanced QM APFD/6-31G* model chemistry, as well as with the force field developed in the present work, and those previously developed by other researchers. Our force field results are almost identical to those of QM calculations. The energy barrier differences (g ↔ o, o ↔ a) between QM and the new force field were minimal, suggesting a realistic representation of the conformational landscape. In addition, we have compared results from previously developed force field parameters with their QM-derived counterpart values in Table 7.

The energy plots for the *trans* conformation (t^+) from Okada et al. [10] and the n-C_4F_{10} specific and generalized perfluoroalkane OPLS-AA force field [18] agree with the QM results. However, both approaches failed to accurately reproduce the *gauche* conformations barrier (g^+, g^-). Okada et al.'s force field calculated higher energy for the *gauche* conformer (0.73 kcal/mol) and significantly higher energy differences, shown in Table 7, at the barriers for g ↔ o (0.79 kcal/mol) and o ↔ a (0.72 kcal/mol), indicating a less favorable description of the potential energy surface compared to other methods. Watkins and Jorgensen [18] extended HF/6-31G model chemistry to derive n-C_4F_{10}-specific force field parameters by including polarization functions (indicated by the asterisk "*"). They also used LMP2/cc-pVTZ(-f) model chemistry to derive generalized perfluoroalkane parameter sets. Their force field performance for n-C_4F_{10} was better than that of Okada et al. regarding energy differences. However, both parameter sets failed to reproduce conformation barriers accurately, as shown in Figure 4(a).

Jang et al.'s [13] force field sets, determined using the Dreiding-type valence potential, provided a satisfactory description of the lower energy differences and barriers, with *gauche* at 0.45 kcal/mol and barriers (g ↔ o: 0.05 kcal/mol), suggesting good accuracy. However, they reported that the g^+ and g^- conformational sets were unstable at the onset of bending torsion angle values for longer PTFE chains. This raises doubts about the transferability of these parameters and their reproduction of macroscopic properties because the authors have not provided any information on whether the force field parameters can predict macroscopic properties. Borodin et al.'s [20] parameter sets also provided a good

Table 4: Optimized bond parameters for PTFE

Bond	K_r (kcal(mol Å^2))$^{-1}$	r_{eq} (Å)
CF_2–CF_2	251.4064	1.5898
CF_2–CF_3	251.4064	1.5898
CF_2–F	361.8779	1.3363
CF_3–F	361.8779	1.3363

Table 5: Optimized angle parameters for PTFE

Angle	K_θ (kcal/(mol radian^2))	θ_{eq}(°)
CF_2–CF_2–CF_2	85.7729	110.9681
F–CF_3–F	99.9229	109.3269
CF_2–CF_3–F	69.8039	108.5623
CF_3–CF_2–F	69.8039	108.5623
CF_2–CF_2–F	69.8039	108.5623
CF_2–CF_2–CF_3	85.7729	110.9681
F–CF_2–F	99.9229	109.3269

Table 6: Optimized dihedral parameters for PTFE

Dihedral	Divider	v_n(kcal/mol)	γ	n
CF_2–CF_2–CF_2–CF_2	1	−1.1301	0.0	−3.0
CF_2–CF_2–CF_2–CF_2	1	0.3810	0.0	−1.0
CF_2–CF_2–CF_2–CF_2	1	4.3339	180.0	2.0
CF_2–CF_2–CF_2–CF_3	1	−1.1301	0.0	−3.0
CF_2–CF_2–CF_2–CF_3	1	0.3810	0.0	−1.0
CF_2–CF_2–CF_2–CF_3	1	4.3339	180.0	2.0
CF_2–CF_2–CF_2–F	1	−0.3651	0.0	−3.0
CF_2–CF_2–CF_2–F	1	13.2574	0.0	−1.0
CF_2–CF_2–CF_2–F	1	0.9940	180.0	2.0
CF_2–CF_2–CF_3–F	1	−0.3651	0.0	−3.0
CF_2–CF_2–CF_3–F	1	13.2574	0.0	−1.0
CF_2–CF_2–CF_3–F	1	0.9940	180.0	2.0
CF_3–CF_2–CF_2–F	1	−0.3651	0.0	−3.0
CF_3–CF_2–CF_2–F	1	13.2574	0.0	−1.0
CF_3–CF_2–CF_2–F	1	0.9940	180.0	2.0
F–CF_2–CF_2–F	1	0.0469	0.0	−3.0
F–CF_2–CF_2–F	1	18.2421	0.0	−1.0
F–CF_2–CF_2–F	1	1.1050	180.0	2.0
F–CF_2–CF_3–F	1	0.0469	0.0	−3.0
F–CF_2–CF_3–F	1	18.2421	0.0	−1.0
F–CF_2–CF_3–F	1	1.1050	180.0	2.0

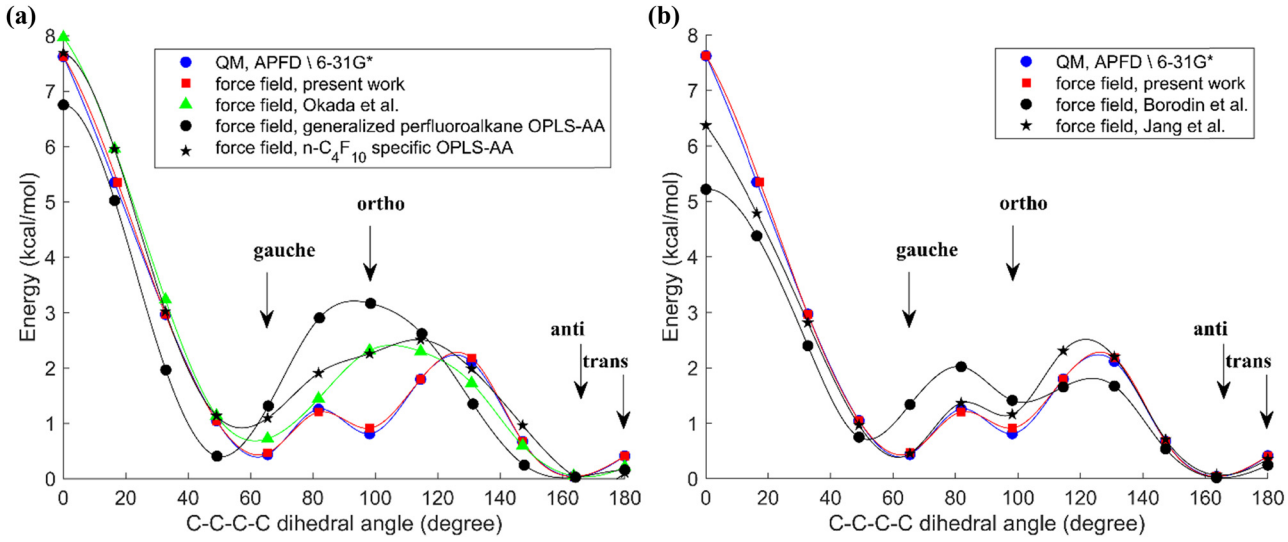

Figure 4: Torsional energy versus C–C–C–C dihedral angle for *n*-C_4F_{10} (a) from QM APFD/6-31G* calculations (blue circles) and the new AMBER force field presented here (squares); both of those data sets are results of the present work, and they are compared to calculations using the Okada et al. force field (triangles) [10], the generalized perfluoroalkane OPLS-AA force field (black circles) [18], and the *n*-C_4F_{10} specific OPLS force field (stars) [18]. Panel (b) shows the same two data sets produced in the present work, and compares them to calculations using the force fields from Jang et al. (stars) [13] and Borodin et al. (black circles) [20].

description of the g^+, g^-, and t^+ conformations for *n*-C_4F_{10}, reproducing torsional energy compared to QM calculations. However, their thermodynamic data, including density and heat of vaporization, were less precise compared to the present work (see below).

3.3 vdW parameters

Optimized vdW interaction parameters are presented in Table 8.

After vdW parameters were optimized, we calculated the heat of vaporization using

$$\Delta H_{\text{vap}}(T,P) = \langle H_{\text{gas}}(T,P)\rangle - \langle H_{\text{liq}}(T,P)\rangle + RT, \qquad (7)$$

where $\langle H_{\text{gas}}(T,P)\rangle$ represents the average total energy of the system in the vapor phase, $\langle H_{\text{liq}}(T,P)\rangle$ represents the average total energy of the system in the liquid phase, R denotes the ideal gas constant, and T is the absolute temperature. The total energy included contributions from bonded and nonbonded interactions and kinetic energy. NPT simulations were conducted at 200, 273, and 298 K with a pressure of 101.3 kPa to calculate the average total energy in both liquid

Table 7: Comparison of the relative conformational energy differences (kcal/mol) of *gauche* (g), *ortho* (o), *anti* (a), and *trans* (t) for C_4F_{10} as a function of the C–C–C–C torsional angle, using various force fields and their QM-derived counterpart values, including those from the present work [a], Okada et al. [10], the *n*-C_4F_{10} specific and generalized perfluoroalkane OPLS-AA force field [18], Jang et al. [13], and Borodin et al. [20]

Model chemistry (QM) & force fields (FF)	ref.	*gauche*	g ↔ o	*ortho*	o ↔ a	*anti*	*trans*
QM → APFD/6-31G*	[a]	0.44	1.24	0.91	2.14	0.00	0.41
FF → Present work	[a]	0.46	1.21	0.84	2.18	0.00	0.40
QM → HF/6-31G	[10]	0.76	2.25	2.05	2.45	0.00	0.14
FF → Okada et al.	[10]	0.73	1.46	2.33	1.73	0.00	0.11
QM → HF/6-31G*	[18]	0.80	2.10	1.90	2.40	0.00	0.10
FF → OPLS-AA (*n*-C_4F_{10} specific)	[18]	1.10	1.91	2.27	1.97	0.00	0.06
FF → OPLS-AA (generalized perfluoroalkane)	[18]	1.31	2.91	3.17	1.35	0.00	0.16
QM → B3LYP/6-31G*	[13]	0.50	1.42	1.17	2.06	0.00	0.39
FF → Jang et al.	[13]	0.45	1.37	1.16	2.19	0.00	0.36
QM → MP2/aug-cc-pvDz	[20]	1.18	1.95	1.55	1.92	0.00	0.11
FF → Borodin et al.	[20]	1.32	2.02	1.42	1.68	0.00	0.25

ref.: reference number, *gauche* (g): *gauche* energy. g ↔ o- energy difference between *gauche* and *ortho*, *ortho* (o): *ortho* energy. o ↔ a: energy difference between *ortho* and *anti*, *anti* (a): *anti*-energy, *trans* (t): *trans* energy, [a] present work.

Table 8: Optimized vdW parameters for PTFE

vdW	ϵ (kcal/mol)	σ (nm)
F	2.8486	0.0634
CF_3	3.1499	0.0838
CF_2	3.2340	0.0781

and gas phases, with 50 molecules in the liquid phase and 1 in the gas phase. Our results for the heat of vaporization and density were compared with the experimental data and results from other force fields in Figure 5.

The density of n–C_4F_{10}, as presented in Figure 5(a) (in g/cm^3), found at 273 K, is 1.591. This performs better than the parameter sets from Jang et al. (1.650) [13], Borodin et al. (1.569) [20], and OPLS-AA (1.581) [18] but is nearly identical to the experimental value of 1.592 reported in the study of Brown and Mears [31]. At another temperature point, 200 K, the density we obtained is 1.820, compared with the experimental density of 1.810 [31]. This is better than the value from Borodin et al. (1.785) [20]. Our result for the heat of vaporization (kcal/mol), as presented in Figure 5(b), is 5.450 at a temperature of 273 K. This value is in close agreement with the experimental value of 5.460, as in the study of Brown and Mears [31]. This level of accuracy signifies an improvement over the results obtained using the parameter sets reported by Okada et al. (5.540) [10] and Borodin et al. (5.920) [20], indicating that our methodology provides a more precise match to the heat of vaporization data. However, even though the density is improved, the calculated heat of vaporization value at 273 K is the same as that obtained using the OPLS-AA force field. At 200 and 298 K, we could not compare the values we calculated due to a lack of experimental and previous force field data.

4 Validation procedures

Validations described in this section involved executing MD simulations in NPT or NVT equilibrium ensembles. For all of these simulations, the time step used was 2.0 fs, and short-range interactions were computed using LJ potentials with a 10 Å cutoff, supplemented with a dispersion correction to account for contributions to energy and pressure from long-range interactions. Beyond this distance, interactions were either ignored or handled using long-range correction methods to reduce computational cost while maintaining accuracy. Additionally, nonbonded interactions between atoms connected by three bonds or fewer were not computed to further streamline the calculations. Arithmetic (for length parameters) and geometric (for energy parameters) averaging rules were used to calculate LJ interactions. The simulation utilized the particle mesh Ewald [44] method to handle electrostatic interactions, coupled with the Nose–Hoover thermostat [45,46] to maintain the desired temperature (unless specified otherwise, simulations below were at T = 300 K). The Parrinello–Rahman approach [47] to regulate pressure at 1 bar was used in NPT ensembles.

4.1 Density distribution

This validation aims to transfer the derived AMBER force field parameters to PTFE models with varying molecular weights to determine the average density distribution in specific regions of these models and compare them against experimental density data to evaluate the accuracy and reliability of the derived force field parameters. Therefore, the QuantumATK molecular simulation software [48] was first utilized with the Monte Carlo method using the OPLS

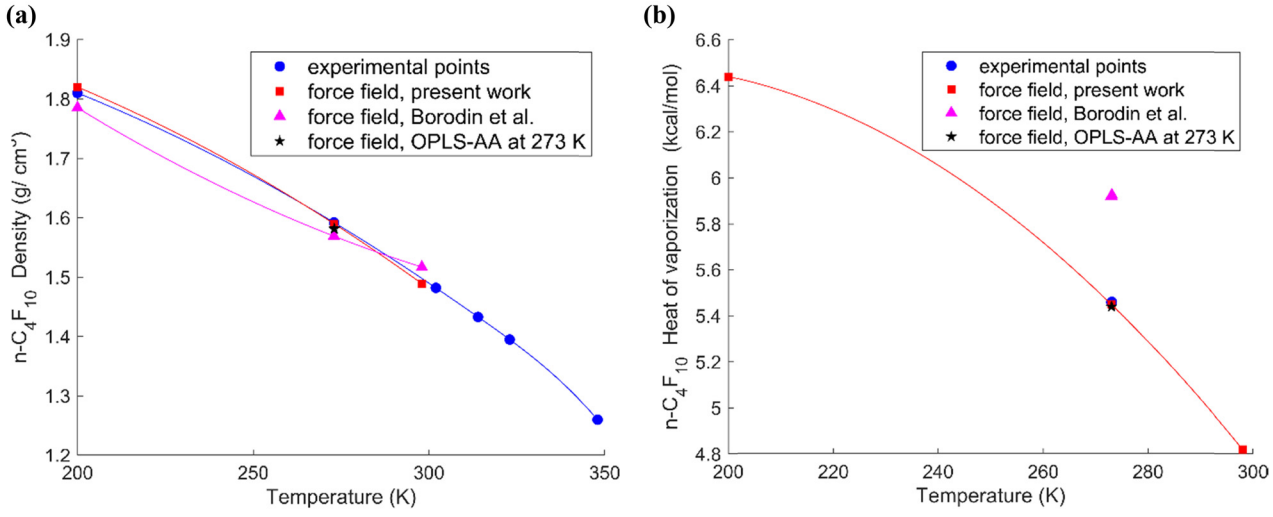

Figure 5: Variation of density (a) and heat of vaporization (b) with temperature for n-C_4F_{10}.

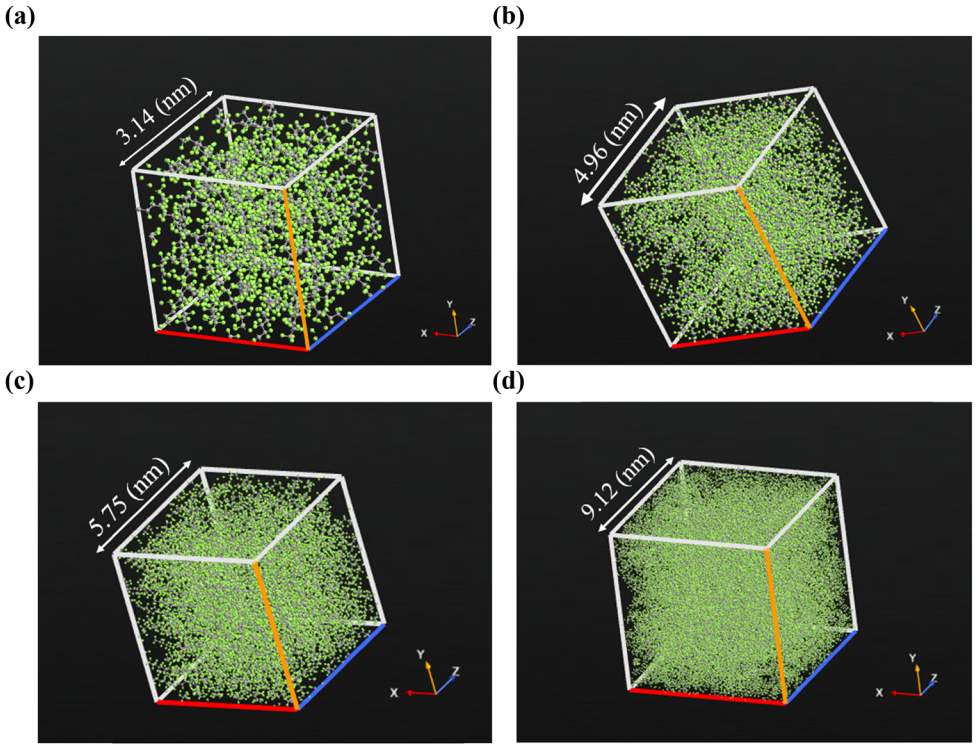

Figure 6: The equilibrated cubic PTFE ensembles of varying size: (a) $[CF_3\text{-}(C_2F_4)_{20}\text{-}CF_3]_{20}$, (b) $[CF_3\text{-}(C_2F_4)_{40}\text{-}CF_3]_{40}$, (c) $[CF_3\text{-}(C_2F_4)_{50}\text{-}CF_3]_{50}$, and (d) $[CF_3\text{-}(C_2F_4)_{100}\text{-}CF_3]_{100}$.

Potential Builder tool [49] to create PTFE models in varying sizes: $[CF_3\text{-}(C_2F_4)_{20}\text{-}CF_3]_{20}$ (this chemical configuration describes a polymer made up of 20 repeating units of a $(CF_3\text{-}(C_2F_4)_{20}\text{-}CF_3)$ chain. Each chain consists of a CF_3 group, followed by 20 repeating units of C_2F_4 (tetrafluoroethylene), and another CF_3 group at the other end), $[CF_3\text{-}(C_2F_4)_{40}\text{-}CF_3]_{40}$, $[CF_3\text{-}(C_2F_4)_{50}\text{-}CF_3]_{50}$, and $[CF_3\text{-}(C_2F_4)_{100}\text{-}CF_3]_{100}$. Then, the Force-Capped MD technique implemented in the QuantumATK software [48] was selected to model PTFE, aiming to mitigate concerns regarding atom overlap or artificially closed atoms within the system. Once the models with variable weights were created, the ACPYPE [50], a Python 3 tool, was employed to convert the force field from AMBER to GROMACS topology files. Then, all MD simulations were executed using GROMACS [39] to obtain the densities and radial distribution function (RDF) from well-equilibrated GROMACS trajectories. To probe if density variations existed within each molecular weight ensemble, density was first computed by dividing each system into slabs along the z-direction. Density in each slab was computed as $\rho = m/V$, where ρ is the density, m is the total mass of the atoms in that slab, and V is the volume of the slab. The average density in different subregions of each ensemble was compared, and no systematic variations were detected. For each ensemble, slab density data were averaged to determine the final density for that molecular weight. These results were then compared with experimental data and previous simulations. Visualizations and results are presented in Figure 6 and Table 9, respectively.

Bhowmik et al. [23] conducted MD simulations of PTFE using GAFF parameters [22] for five chain lengths and reported a predicted density of 1,820 kg/m^3. Okada et al. [10] performed MD simulations on amorphous PTFE assemblies and observed a predicted 1,900 kg/m^3 density. The percentage of errors reported by Bhowmik et al. and Okada et al. was significantly higher than that of the present study.

4.2 RDF

The pair-specific spherical atomic RDFs $g_{CF}(r)$ were calculated to determine the coordination of fluorine (F) atoms around carbon (C) atoms over a GROMACS trajectory using the VMD GUI Plugin [51]. The RDF is determined by measuring the distances between atoms or particles within specified groups. These distance data are then converted into a histogram, where the occurrences of particles at various distances are counted. To obtain the RDF, the counts in the histogram are divided by the average density.

Table 9: Comparison of our density values from MD simulations of various-sized PTFE ensembles, with MD simulations using Okada et al. [10] and GAFF force field parameters [22], with the experimental density at 300 K reported in the study of Nunes et al. [32]

Molecular weights	$[CF_3\text{-}(C_2F_4)_{20}\text{-}CF_3]_{20}$	$[CF_3\text{-}(C_2F_4)_{40}\text{-}CF_3]_{40}$	$[CF_3\text{-}(C_2F_4)_{50}\text{-}CF_3]_{50}$	$[CF_3\text{-}(C_2F_4)_{100}\text{-}CF_3]_{100}$	Okada force field	GAFF force field	Experimental value
Density (kg/m^3)	2,151	2,201	2,171	2,161	1,900	1,820	2,180
Percent error (%)	1.4	0.9	0.4	0.8	13	17	0

The mathematical expression for the RDF, $g_{CF}(r)$, is as follows:

$$g_{CF}(r) = \frac{\rho_{CF}(r)}{\rho_C \cdot \rho_F \cdot (4\pi r^2) \cdot \Delta r}. \tag{8}$$

$g_{CF}(r)$ characterizes the spatial arrangement of F atoms around C atoms in a given system. It represents the probability of encountering an F atom located at a specific distance "r" from a C atom, normalized based on the system's average C and F atom density. The number density of F atoms around a C atom at distance "r" is denoted by $\rho_{CF}(r)$, while ρ_C and ρ_F refer to the densities of C and F in the assembled system. The width of the spherical shell (bin size), denoted as Δr, is used to accumulate atoms within a distance range from "r" to "$r + \Delta r$," and the surface area of this shell is given by $4\pi r^2$. The RDF results depicted in Figure 7 show that the PTFE system's atomic interactions and structural properties remain relatively consistent and do not significantly alter with changes in ensemble size and/or molecular weight. Si et al. [52] observed that the pure amorphous PTFE peaks appear around $2\Theta = 18°$, 33°, 37°, 49°, 56°, 67°, and 69° in X-ray diffraction experiments using Cu-Kα radiation. These peaks match those in the RDF at 4.94, 2.73, 2.42, 1.86, 1.65, 1.38, and 1.36 Å, respectively. These peak values were compared with the calculated ones shown in Figure 7.

4.3 Power spectrum

The power spectrum or velocity density of states (VDOS) is calculated using data from an MD simulation according to the study of Agarwal et al. [53] as follows:

$$P(\omega) = \int_{-\infty}^{+\infty} C(t) e^{i\omega t} dt, \tag{9}$$

where $C(t)$ is the normalized velocity autocorrelation function (VACF). The calculation of the $C(t)$ is as follows:

$$C(t) = \sum_{i=1}^{m} v_k(i) v_k(i+n) / \sum_{i=1}^{m} v_k(i) v_k(i). \tag{10}$$

The $v_k(i)v_k(i+n)$ term represents the correlation between the velocity at time $i{\cdot}\Delta t$ and the velocity at time $(i+n){\cdot}\Delta t$. $v_k(i)v_k(i)$ is the correlation of the velocity with itself, and m is the total number of time steps over which the correlation will be computed. v_k is the velocity associated with a specific wave vector in Fourier space defined as

$$v_k(t) = \sum_j u_j(t) e^{ikx_j^0}. \tag{11}$$

The $u_j(t)$ is the velocity vector of the jth atom at time t. The $e^{ikx_j^0}$ is the complex exponential function, where $k = \frac{2\pi}{\lambda}$ is the wave vector, and x_j^0 is defined as the initial position or reference position of the jth atom. The wave vector (k) specifies the wave's spatial frequency direction and is inversely related to the wavelength (λ) of the wave. By summing over all particles and multiplying each particle's displacement $u_j(t)$ by the complex exponential factor $e^{ikx_j^0}$, one can obtain the combined effect of each particle's contribution to the velocity associated with wave vector k at time t [54]. To compute the power spectrum from the VACF, MD simulations were performed using periodic boundary conditions in a cubic box with an edge length of 200 Å using GROMACS software [39]. The simulations included a chain composed of 50 n-C_4F_{10} reference molecules. The

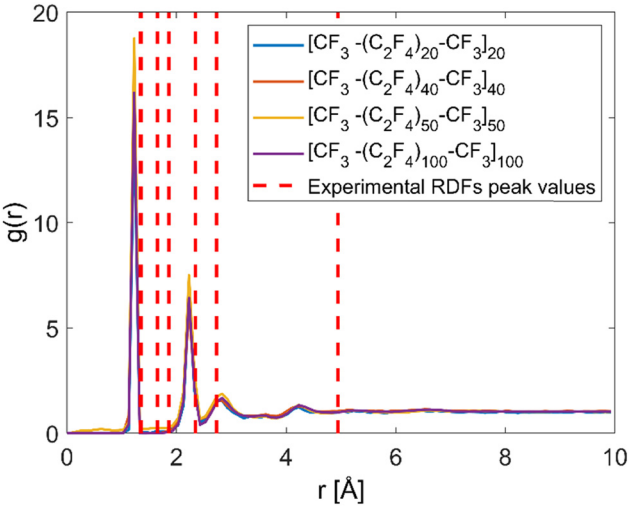

Figure 7: Comparison of experimental RDF peak values with RDFs for equilibrated cubic PTFE ensembles of various sizes: $[CF_3\text{-}(C_2F_4)_{20}\text{-}CF_3]_{20}$.

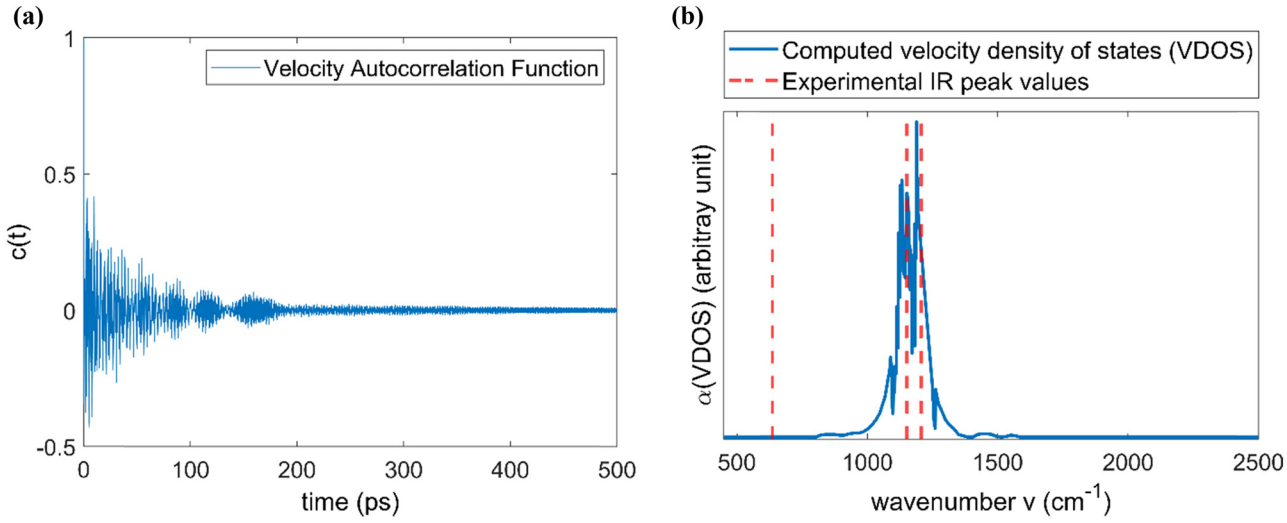

Figure 8: (a) Temporal variation of the VACF. (b) VDOS or power spectrum of the PTFE chain (500–2,500 cm^{-1}) with experimental peak points shown by the red dashed lines.

system's energy was first minimized over 10,000 steps using the steepest descent algorithm. Then, an NPT simulation ran for 1.2 ns (nanoseconds) to adjust box length/density. Next, NVT simulations at T = 300 K were conducted using a box size from the previous NPT step to equilibrate the system further. After NVT equilibration, power spectra were calculated over 200 ps of analysis time. The temporal variation of the VACF results is shown in Figure 8(a). Figure 8(b) compares the VDOS results with the experimental infrared spectrum. The peak positions of the calculated VDOS closely correspond to those observed in the experimental infrared spectrum obtained from the study of Wang et al. [33].

The temporal variation of the VACF (Figure 8(a)) illustrates the evolving correlation between velocities over time. Experimental peak values, indicated by red dashed lines in Figure 8b, were compared with values obtained from MD simulations. Four prominent peaks were observed at wavenumbers 1,207, 1,151, 638, and 626 cm^{-1} in the experimental infrared spectrum of PTFE fibers [33]. The peak at 638 cm^{-1} in the experimental spectrum was attributed to a regular helix structure. In contrast, the peak at 626 cm^{-1} was linked to a helix-reversal defect in PTFE fibers, which was not observed in the MD simulation results [55]. The bands at 1,207 and 1,151 cm^{-1} were previously considered insensitive to the crystallinity level [56]. These bands have been attributed to the symmetric and asymmetric stretching vibrations of CF_2 and C–C groups within the PTFE fibers. The computed peak positions of 1,189 and 1,132 cm^{-1} closely matched the experimental study's peak positions of 1,207 and 1,151 cm^{-1}, with deviations of 18 and 19 cm^{-1}, respectively.

4.4 Specific heat capacity

The specific heat ($C_p(T)$), or heat capacity per mass unit, was calculated based on the PTFE assemblies' vibrational modes at constant volume across temperatures using QuantumATK. The expression of $C_p(T)$ is described by the following formula [57]:

$$C_p(T) = \frac{h^2}{mk_BT^2}\int_0^\infty \frac{v^2 \exp\left(\frac{hv}{k_BT}\right)}{\left(\exp\left(\frac{hv}{k_BT}\right)-1\right)^2} g(v)\mathrm{d}v, \qquad (12)$$

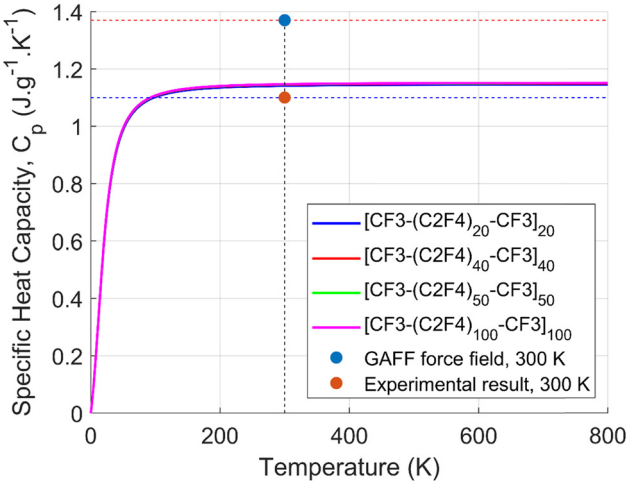

Figure 9: Comparison of computed and experimental specific heat capacity vs temperature for different ensembles of various sizes: $[CF_3\text{-}(C_2F_4)_{20}\text{-}CF_3]_{20}$, $[CF_3\text{-}(C_2F_4)_{40}\text{-}CF_3]_{40}$, $[CF_3\text{-}(C_2F_4)_{50}\text{-}CF_3]_{50}$, and $[CF_3\text{-}(C_2F_4)_{100}\text{-}CF_3]_{100}$.

where T represents the temperature, ν denotes the vibrational frequency, h stands for Planck's constant, m indicates the total mass of the atoms in the unit cell, k_B represents Boltzmann's constant, and $g(\nu)$ symbolizes the vibrational density of states, which describes how energy is distributed among vibrational modes [58]. The integral in the formula calculates the contribution of each vibrational mode to the specific heat, weighted by $g(\nu)$. The fraction within the integral represents the population of each vibrational mode at temperature T, as described by the Bose–Einstein distribution. The factor, $h^2/(2\pi m k_B T)^2$, positioned outside the integral, normalizes the units and scales the result appropriately. For this analysis, after the NPT equilibration described in the preceding section, MD simulations were executed under the NVT ensemble, wherein the temperature ranged from 0 to 800 K in increments of 100 K over a total duration of 3 ns, followed by a 1 ns duration at 800 K. After that, the temperature decreased to 300 K with the cooling rate of 4 K/ps and held for another 1 ns. Specific heat capacity was calculated during this entire MD trajectory using QuantumATK [48]. Our calculations yielded a heat capacity of 1.15 ($J\,g^{-1}\,K^{-1}$) with a percent error of 4.5% based on MD simulations performed on four distinct assemblies of PTFE. This result closely aligns with the experimental findings of 1.10 ($J\,g^{-1}\,K^{-1}$) reported by Furukawa et al. [34] (Figure 9). Additionally, Bhowmik et al. [23] conducted MD simulations using standard GAFF parameters [22] to predict the specific heat across various sizes of PTFE ensembles at only 300 K. Therefore, only 300 K comparisons were made. Their computational estimate was 1.37 ($J\,g^{-1}\,K^{-1}$), with a reported percent error of 24.5%, significantly higher than our calculated value.

5 Conclusions

We introduce a new force field parameter set for PTFE, generated using the Paramfit protocol to optimize the bonded AMBER force field parameters. The optimization procedure involved refining conformational sets and fine-tuning the vdW parameters based on experimental data. These parameters showed excellent agreement with experimental data, particularly in reproducing the density and heat of vaporization of PTFE. The transferability of our force field parameters was demonstrated by simulating PTFE systems of different molecular weights. The resultant parameters exhibited high accuracy in predicting the density and specific heat capacity for various molecular weights of PTFE ensembles and the peak vibration spectrum values of the PTFE chain. This was coupled with the close agreement observed between the derived MM parameters and their corresponding QM references, as well as with experimental data. Overall, the force field parameters developed in this study represent a significant improvement over existing models in the literature, offering high accuracy and reliability for simulating PTFE and facilitating a better understanding of its behavior at the molecular level.

Acknowledgments: The computational results presented in this study were partly performed on Lehigh University Research Computing Infrastructure, the Sol and Hawk high-performance computing clusters. Hawk was made possible by NSF Grant 2019035.

Funding information: The authors have stated that no funding was involved.

Author contributions: Orhan Kaya: conceptualization, data curation, methodology, validation, visualization, formal analysis, and writing – original draft. Alparslan Oztekin: supervision, formal analysis, and writing – review and editing. Edmund B. Webb III: supervision, resources, formal analysis, writing – review and editing.

Conflict of interest: The authors declare no conflict of interest.

Ethical approval: The conducted research is not related to either human or animal use.

Data availability statement: The AMBER force field parameters generated during the current study, as well as the parameters converted to LAMMPS and GROMACS formats, are available on Figshare and accessible via the following persistent web link: https://doi.org/10.6084/m9.figshare.26197325.v1.

References

[1] Adnan S, Hoang M, Wang H, Xie Z. Commercial PTFE membranes for membrane distillation application: Effect of microstructure and support material. Desalination. 2012 Jan;284:297–308. doi: 10.1016/j.desal.2011.09.015.

[2] Jiang H, Fang H, Wang D, Sun J. Spray-Coated Commercial PTFE Membrane from MoS_2/LaF_3/PDMS Ink as Solar Absorber for Efficient Solar Steam Generation. Sol RRL. 2020 Jun;4(6):2000126. doi: 10.1002/solr.202000126.

[3] Lee M-K, Park C, Jang T-S, Kim H-E, Jeong S-H. Enhanced mechanical stability of PTFE coating on nano-roughened NiTi for biomedical applications. Mater Lett. 2018 Apr;216:12–5. doi: 10.1016/j.matlet.2017.12.139.

[4] Kameda T, Ohkuma K, Oka S. Polytetrafluoroethylene (PTFE): A resin material for possible use in dental prostheses and devices. Dent Mater J. 2019 Jan;38(1):136–42. doi: 10.4012/dmj.2018-088.

[5] Patel NA, Shah P, Yannuzzi NA, Ansari Z, Zaveri JS, Relhan N, et al. Clinical outcomes of 4-point scleral fixated 1-piece hydrophobic acrylic equiconvex intraocular lens using polytetrafluoroethylene suture. Clin Ophthalmol. 2018 Oct;12:2145–8. doi: 10.2147/OPTH.S174211.

[6] Labroo P, Hilgart D, Davis B, Lambert C, Sant H, Gale B, et al. Drug-delivering nerve conduit improves regeneration in a critical-sized gap. Biotechnol Bioeng. 2019 Jan;116(1):143–54. doi: 10.1002/bit.26837.

[7] Gross U, Papke G, Rüdiger S. Fluorocarbons as blood substitutes: critical solution temperatures of some perfluorocarbons and their mixtures. J Fluor Chem. 1993 Mar;61(1–2):11–6. doi: 10.1016/S0022-1139(00)80411-X.

[8] Ebnesajjad S. Fluorine and fluorocarbons. In: Introduction to fluoropolymers. Amsterdam, Netherlands: Elsevier Science; 2013. p. 5–15. doi: 10.1016/B978-1-4557-7442-5.00002-4.

[9] Foresman JB, Frish AE. Exploring chemistry with electronic structure methods. 3rd edn. Wallingford, CT: Gaussian, Inc.

[10] Okada O, Oka K, Kuwajima S, Tanabe K. Molecular dynamics studies of amorphous poly(Tetrafluoroethylene). Mol Simul. 1999 Jan;21(5–6):325–42. doi: 10.1080/08927029908022072.

[11] Curtiss LA, Raghavachari K, Redfern PC, Rassolov V, Pople JA. Gaussian-3 (G3) theory for molecules containing first and second-row atoms. J Chem Phys. 1998 Nov;109(18):7764–76. doi: 10.1063/1.477422.

[12] Dunning TH. Gaussian basis sets for use in correlated molecular calculations. I. The atoms boron through neon and hydrogen. J Chem Phys. 1989 Jan;90(2):1007–23. doi: 10.1063/1.456153.

[13] Jang SS, Blanco M, Goddard WA, Caldwell G, Ross RB. The source of helicity in perfluorinated *N*-alkanes. Macromolecules. 2003 Jul;36(14):5331–41. doi: 10.1021/ma025645t.

[14] Becke AD. Density-functional thermochemistry. III. The role of exact exchange. J Chem Phys. 1993 Apr;98(7):5648–52. doi: 10.1063/1.464913.

[15] Lee C, Yang W, Parr RG. Development of the Colle-Salvetti correlation-energy formula into a functional of the electron density. Phys Rev B. 1988 Jan;37(2):785–9. doi: 10.1103/PhysRevB.37.785.

[16] Dasgupta S, Yamasaki T, Goddard WA. The Hessian biased singular value decomposition method for optimization and analysis of force fields. J Chem Phys. 1996 Feb;104(8):2898–920. doi: 10.1063/1.471112.

[17] Mulliken RS. Electronic population analysis on LCAO–MO molecular wave functions. I. J Chem Phys. 1955 Oct;23(10):1833–40. doi: 10.1063/1.1740588.

[18] Watkins EK, Jorgensen WL. Perfluoroalkanes: Conformational analysis and liquid-state properties from ab initio and Monte Carlo calculations. J Phys Chem A. 2001 Apr;105(16):4118–25. doi: 10.1021/jp004071w.

[19] Vaara J, Malkina OL, Stoll H, Malkin VG, Kaupp M. Study of relativistic effects on nuclear shieldings using density-functional theory and spin–orbit pseudopotentials. J Chem Phys. 2001 Jan;114(1):61–71. doi: 10.1063/1.1330208.

[20] Borodin O, Smith GD, Bedrov D. A quantum chemistry based force field for perfluoroalkanes and poly(tetrafluoroethylene). J Phys Chem B. 2002 Sep;106(38):9912–22. doi: 10.1021/jp026158i.

[21] Møller C, Plesset MS. Note on an approximation treatment for many-electron systems. Phys Rev. 1934 Oct;46(7):618–22. doi: 10.1103/PhysRev.46.618.

[22] Wang J, Wolf RM, Caldwell JW, Kollman PA, Case DA. Development and testing of a general amber force field. J Comput Chem. 2004 Jul;25(9):1157–74. doi: 10.1002/jcc.20035.

[23] Bhowmik R, Sihn S, Varshney V, Roy AK, Vernon JP. Calculation of specific heat of polymers using molecular dynamics simulations. Polymer. 2019 Mar;167:176–81. doi: 10.1016/j.polymer.2019.02.013.

[24] Austin A, Petersson GA, Frisch MJ, Dobek FJ, Scalmani G, Throssell K. A density functional with spherical atom dispersion terms. J Chem Theory Comput. 2012 Dec;8(12):4989–5007. doi: 10.1021/ct300778e.

[25] Hansen PE, Saeed BA, Rutu RS, Kupka T. One-bond $^{1}J(^{15}\mathrm{N,H})$ coupling constants at sp^2-hybridized nitrogen of Schiff bases, enaminones and similar compounds: A theoretical study. Magn Reson Chem. 2020 Aug;58(8):750–62. doi: 10.1002/mrc.5052.

[26] Malloum A, Fifen JJ, Conradie J. Solvation energies of the proton in methanol revisited and temperature effects. Phys Chem Chem Phys. 2018;20(46):29184–206. doi: 10.1039/C8CP05823G.

[27] Bayly CI, Cieplak P, Cornell W, Kollman PA. A well-behaved electrostatic potential based method using charge restraints for deriving atomic charges: the RESP model. J Phys Chem. 1993 Oct;97(40):10269–80. doi: 10.1021/j100142a004.

[28] Frisch MJ, Trucks GW, Schlegel HB. Gaussian 16, Revision C.01. Wallingford CT: Gaussian, Inc.; 2016.

[29] Wang J, Wang W, Kollman PA, Case DA. Automatic atom type and bond type perception in molecular mechanical calculations. J Mol Graph Model. 2006 Oct;25(2):247–60. doi: 10.1016/j.jmgm.2005.12.005.

[30] Betz RM, Walker RC. Paramfit: Automated optimization of force field parameters for molecular dynamics simulations. J Comput Chem. 2015 Jan;36(2):79–87. doi: 10.1002/jcc.23775.

[31] Brown JA, Mears WH. Physical properties of *n*-Perfluorobutane. J Phys Chem. 1958 Aug;62(8):960–2. doi: 10.1021/j150566a015.

[32] Nunes LCS, Dias FWR, Da Costa Mattos HS. Mechanical behavior of polytetrafluoroethylene in tensile loading under different strain rates. Polym Test. 2011 Oct;30(7):791–6. doi: 10.1016/j.polymertesting.2011.07.004.

[33] Wang R, Xu G, He Y. Structure and properties of polytetrafluoroethylene (PTFE) fibers. E-Polym. 2017 May;17(3):215–20. doi: 10.1515/epoly-2016-0059.

[34] Furukawa GT, Mccoskey RE, King GJ. Calorimetric properties of polytetrafluoroethylene (teflon) from 0-degrees to 365-degrees-K. J Res Natl Bur Stand. 1952 Oct;49(4):273. doi: 10.6028/jres.049.029.

[35] Hanwell MD, Curtis DE, Lonie DC, Vandermeersch T, Zurek E, Hutchison GR. SOFTWARE Open Access Avogadro. London, United Kingdom: BioMed Central; 2012.

[36] Case DA, Aktulga HM, Belfon K, Cerutti DS, Cisneros GA, Cruzeiro VW, et al. AmberTools. J Chem Inf Model. 2023 Oct;63(20):6183–91. doi: 10.1021/acs.jcim.3c01153.

[37] Hopkins CW, Roitberg AE. Fitting of dihedral terms in classical force fields as an analytic linear least-squares problem. J Chem Inf Model. 2014 Jul;54(7):1978–86. doi: 10.1021/ci500112w.

[38] PubChem Compound Summary for CID 9638, Perflubutane; 2024. [Online]. Available: https://pubchem.ncbi.nlm.nih.gov/compound/Perflubutane.

[39] Abraham MJ, Murtola T, Schulz R, Páll S, Smith JC, Hess B, et al. GROMACS: High performance molecular simulations through multi-level parallelism from laptops to supercomputers. SoftwareX. 2015 Sep;1–2:19–25. doi: 10.1016/j.softx.2015.06.001.

[40] Nelder JA, Mead R. A simplex method for function minimization. Comput J. 1965 Jan;7(4):308–13. doi: 10.1093/comjnl/7.4.308.

[41] Faller R, Schmitz H, Biermann O, Moller-Plathe F. Automatic parameterization of force fields for liquids by simplex optimization. J Comput Chem. 1999 Jul;20(10):1009–17. doi: 10.1002/(SICI)1096-987X(19990730)20:10<1009: AID-JCC3>3.0.CO;2-C.

[42] Barton RR, Ivey JS. Modifications of the Nelder-Mead simplex method for stochastic simulation response optimization. In: 1991 Winter Simulation Conference Proceedings. Phoenix, AZ, USA: IEEE; 1991. p. 945–53. doi: 10.1109/WSC.1991.185709.

[43] Tantardini C, Oganov AR. Thermochemical electronegativities of the elements. Nat Commun. 2021 Apr;12(1):2087. doi: 10.1038/s41467-021-22429-0.

[44] Darden T, York D, Pedersen L. Particle mesh Ewald: An *N* ·log(*N*) method for Ewald sums in large systems. J Chem Phys. 1993 Jun;98(12):10089–92. doi: 10.1063/1.464397.

[45] Nosé S. A molecular dynamics method for simulations in the canonical ensemble. Mol Phys. 1984 Jun;52(2):255–68. doi: 10.1080/00268978400101201.

[46] Hoover WG. Canonical dynamics: Equilibrium phase-space distributions. Phys Rev A. 1985 Mar;31(3):1695–7. doi: 10.1103/PhysRevA.31.1695.

[47] Parrinello M, Rahman A. Polymorphic transitions in single crystals: A new molecular dynamics method. J Appl Phys. 1981 Dec;52(12):7182–90. doi: 10.1063/1.328693.

[48] Smidstrup S, Markussen T, Vancraeyveld P, Wellendorff J, Schneider J, Gunst T, et al. QuantumATK: an integrated platform of electronic and atomic-scale modelling tools. J Phys Condens Matter. 2020 Jan;32(1):015901. doi: 10.1088/1361-648X/ab4007.

[49] Schneider J, Hamaekers J, Chill ST, Smidstrup S, Bulin J, Thesen R, et al. ATK-ForceField: a new generation molecular dynamics software package. Model Simul Mater Sci Eng. 2017 Dec;25(8):085007. doi: 10.1088/1361-651X/aa8ff0.

[50] Sousa Da Silva AW, Vranken WF. ACPYPE - AnteChamber PYthon Parser interfacE. BMC Res Notes. 2012 Dec;5(1):367. doi: 10.1186/1756-0500-5-367.

[51] Humphrey W, Dalke A, Schulten K. VMD: Visual molecular dynamics. J Mol Graph. 1996 Feb;14(1):33–8. doi: 10.1016/0263-7855(96)00018-5.

[52] Si J, Ma R, Wu Y, Dong Y, Yao K. Microstructure and magnetic properties of novel powder cores composed of iron-based amorphous alloy and PTFE. J Mater Sci. 2022 May;57(17):8154–66. doi: 10.1007/s10853-022-07199-4.

[53] Agarwal V, Huber GW, Conner WC, Auerbach SM. Simulating infrared spectra and hydrogen bonding in cellulose Iβ at elevated temperatures. J Chem Phys. 2011 Oct;135(13):134506. doi: 10.1063/1.3646306.

[54] Kleinhesselink D, Wolfsberg M. The evaluation of power spectra in molecular dynamics simulations of anharmonic solids and surfaces. Surf Sci. 1992 Feb;262(1–2):189–207. doi: 10.1016/0039-6028(92)90471-H.

[55] Quarti C, Milani A, Castiglioni C. Ab initio calculation of the IR spectrum of PTFE: Helical symmetry and defects. J Phys Chem B. 2013 Jan;117(2):706–18. doi: 10.1021/jp3102145.

[56] Starkweather HW, Ferguson RC, Chase DB, Minor JM. Infrared spectra of amorphous and crystalline poly(tetrafluoroethylene). Macromolecules. 1985 Sep;18(9):1684–6. doi: 10.1021/ma00151a007.

[57] Horbach J, Kob W, Binder K. Specific heat of amorphous silica within the harmonic approximation. J Phys Chem B. 1999 May;103(20):4104–8. doi: 10.1021/jp983898b.

[58] Lin ST, Blanco M, Goddard WA. The two-phase model for calculating thermodynamic properties of liquids from molecular dynamics: Validation for the phase diagram of Lennard-Jones fluids. J Chem Phys. 2003 Dec;119(22):11792–805. doi: 10.1063/1.1624057.